ADVANCED MATERIALS INTERFACES
www.advmatinterfaces.de

Microfluidic Device for Monitoring Catalytic Events on Armored Bubbles

Dmytro Dedovets, Shi Zhang, Jacques Leng, and Marc Pera-Titus**

A polydimethylsiloxane-based microfluidic device allows monitoring local oxidation events in organic solvents at the level of an individual air bubble armored with surface-active low-surface energy catalytic particles. This new technique permits tunable design of microreactors for gas-liquid-solid reactions.

1. Introduction

Gas-liquid-solid (G–L–S) catalytic reactions are ubiquitous in chemical, petrochemical, biochemical, and environmental catalytic processes. The reactions are operated in packed beds (e.g., trickle beds, bubble columns), stirred tanks and bubble column slurry reactors, and fluidized beds.[1] The engineering of G–L–S reactions is however complex due to the low solubility of gases in liquids, and to resilient mass/heat transfer limitations ascribed to the physical separation of the phases. As a result, high gas pressures and the addition of phase transfer reagents are often required. Moreover, access to the intrinsic activity of the catalyst and associated process optimization is not straightforward.

Herein we present a microfluidic device to generate, manipulate and study catalytic events at the level of an individual armored bubble in an organic solvent. Anchoring catalytic particles at the G–L interface can promote locally the G–L–S contact and allow the reaction to occur at a much smaller scale, with the potential enhancement of the G–L miscibility and mass transfer.[2]

Despite the advances in the field of microfluidics, its implementation for preparing monodisperse particle-stabilized emulsions and foams has only been realized recently.[3] While the vast majority of studies have focused on the use of microfluidics in aqueous systems, very few examples of particle-stabilized gas bubbles and foams in organic solvents have been documented.[3,4] Besides, while droplet trapping using microfluidics has been achieved for simple emulsions and gas-core multiple emulsions,[5] transposition of proposed solutions to G–L systems has not been demonstrated so far owing to the low surface tension of organic liquids. As a result, particles with low-surface energy (e.g., fluorinated particles) are required as stabilizers to generate non-aqueous/oil foams and bubbles.[4,6]

2. Results and Discussion

2.1. Synthesis of Fluorinated Catalytic Particles

To prepare particle-stabilized bubbles, we synthesized surface-active silica particles (≈300 nm) bearing fluorinated chains and thiol groups by the Stöber method and loaded them with palladium nanoparticles (average size 5.2 nm, 1.78 wt%).[2] The synthesis protocol and particle characterization results are described in the Supporting Information (Figures S1–S5, Supporting Information). The particles are hereinafter denoted as Pd@SiO_2-F17. Moreover, we prepared non-catalytic fluorescent silica particles incorporating C_{18} alkyl chains and rhodamine B which are denoted as SiO_2-C18-RhB.

2.2. Microfluidic Generation of Particle-stabilized Bubbles

As a rule, particles possess marginal colloidal stability in water and organic solvents, making their use in microfluidics more challenging compared to surfactants: particles are prone to phase separation in the syringe and microfluidic channels, resulting in fouling and clogging of the latter. This is even more stringent in the case of (fluorinated) particles stabilizing G–L systems, showing a larger structural difference between the particles and the liquid phase, to ensure wettability by the gas phase. This brings up a controversy: particles need to be concomitantly surface-active (i.e., partially wetted by both phases) to stabilize bubbles, and colloidally stable (i.e., fully wetted by the solvent) to be compatible with microfluidics.

D. Dedovets, S. Zhang, J. Leng
Laboratoire du Futur (LOF)
UMR 5258 CNRS-Solvay-Univ. Bordeaux, 178 Av. Dr Albert Schweitzer, Pessac Cedex 33608, France
E-mail: jacques.leng-exterieur@solvay.com
M. Pera-Titus
Eco-Efficient Products and Processes Laboratory (E2P2L)
UMI 3464 CNRS-Solvay, 3966 Jin Du Road, Xin Zhuang Ind. Zone, Shanghai 201108, China
E-mail: peratitusm@cardiff.ac.uk
M. Pera-Titus
Cardiff Catalysis Institute
School of Chemistry
Cardiff University
Main Building, Park Place, Cardiff CF10 3AT, UK
The ORCID identification number(s) for the author(s) of this article can be found under https://doi.org/10.1002/admi.202200759.

DOI: 10.1002/admi.202200759

In aqueous foams, tunable wettability can be achieved using pH-sensitive particles.[7] In contrast, for oil foams, particle migration from the bulk to the interface can only be solved by an on-demand change of the particle wettability, which can be triggered by a change in the solvent composition. In this work, we adopted the latter approach to adjust the wettability of Pd@SiO_2-F17 particles and generate bubbles in organic solvents. We dispersed the particles in a "good" solvent and the contact angle was adjusted on-demand by injecting a "bad" co-solvent (**Figure 1**a and Figure S6, Supporting Information). We implemented this approach using a microfluidic chip consisting of a flow-focusing bubble generator in the "good" solvent, followed by a "bad" solvent injector, covering the channel and observation chamber (Figure 1b top). Stable bubbles are produced using a 5 wt% Pd@SiO_2-F17 dispersion in 1-octanol and dimethyl sulfoxide (DMSO) (1:1 v/v) as "good" and "bad" solvents, respectively, at 80 °C using equal flowrates of both solvents (Figure 1b bottom). At these conditions, assuming complete particle adsorption at the G–L interface, the particle coverage is around 250%, whereas it reduces down to 50% using a 1 wt% Pd@SiO_2-F17 dispersion, resulting in poorly stable bubbles (Figure S7, Supporting Information).

Starting from a 5 wt% Pd@SiO_2-F17 particle dispersion, the bubble size can be adjusted without coalescence neither in the observation chamber nor output tube by varying the gas pressure. However, by inversing the injection order of the liquid phases, polydisperse bubbles are generated under most of the experimental conditions (Figure S8, Supporting Information). This difference can be explained by a variable particle concentration near the G-L interface, and by the shear stress provided by the cross-flow during droplet formation.[8] Indeed, when bubbles are first generated in the pure solvent followed by injection of the particle dispersion, particles need to diffuse within the thin film of solvent on the bubble surface, reducing, in turn, their concentration in the vicinity of the G–L interface.

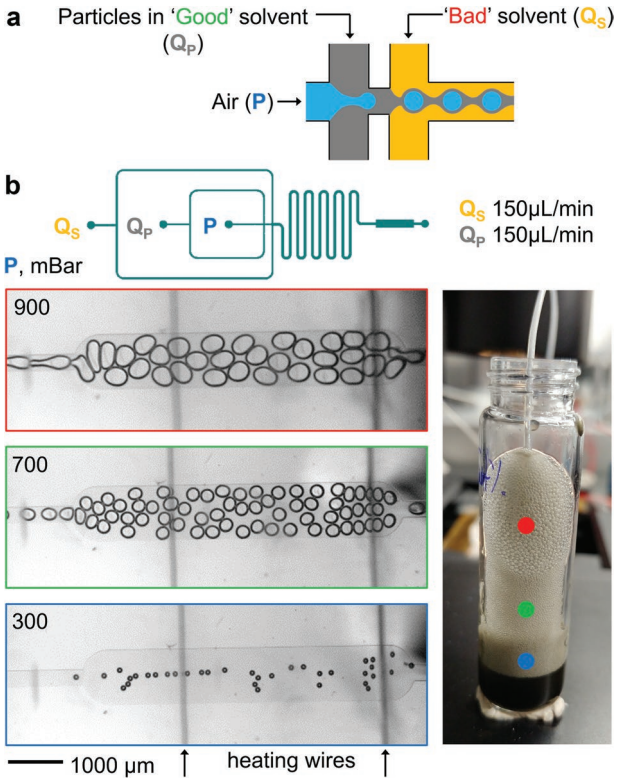

Figure 1. Microfluidic generation of particle-stabilized bubbles. a) Operation principle, b) chip design and high-speed microscopy images. Bubbles are generated in the particle suspension in "good" solvent (Q_p – 5 wt% Pd@SiO_2-F17 in 1-octanol) and "bad" solvent (Q_s _ DMSO) is introduced afterward. Foams marked with colored dots (on the right) are produced at the conditions marked by corresponding rectangles (on the left). Temperature 80 °C.

Interestingly, at high gas pressure (900 mBar), deformation of the bubble shape occurs (Figure S9, Supporting Information). This phenomenon was observed previously for slug bubbles covered by a mixture of silica particles and the surfactant hexadecyltrimethylammonium bromide (CTAB).[9] The drag force exerted on the particles covering the interface (due to viscous effect or solid friction on the wall) tends to migrate the particles toward the rear of the drop, a situation prone to shape instability. The position of the neck indicates the fraction of the bubble covered by the particles.

This approach can be extended to other types of particles with suitable surface chemistry. For instance, bubbles can be generated in the microfluidic channels using 5 wt% non-catalytic SiO_2-C18-RhB particles in octanol/DMSO (1:1) (Figure S10, Supporting Information – middle). This system allows monitoring particle shell formation by fluorescence (Figure 5). An increase of the co-solvent flow rate leads to lower effective particle concentration and in turn to the formation of unstable bubbles (Left of Figure S10, Supporting Information). On the other hand, decreasing the flow rate of the co-solvent results in over-wetting of particles (i.e., contact angle out of the stability zone) and the formation of unstable bubbles (Right of Figure S10, Supporting Information). The flow rate window for stabilizing bubbles, therefore, depends on the pair of solvents and the type of particles used.

2.3. Design of Microfluidic Traps

The residence time of bubbles in the microfluidic channel is very short (30–60 ms in our experiments). Therefore, in order to study the reactivity at the level of an individual bubble, this needs first to be immobilized. While a range of technical solutions is available for trapping emulsion droplets, they can hardly be transposed to bubbles due to the deformability of the latter.[10] Moreover, contrary to emulsions, where the droplet size is (mostly) determined by the flow rate of the two immiscible phases, the bubble size depends strongly on the pressure difference (ΔP) between the gas and liquid phases in G–L systems. Reaching steady state requires the pressure drop to settle downstream of the nozzle (i.e., no coalescence, no interaction with walls, etc.) and this may take long time. However, it is a prerequisite to keep constant the size of the newly generated bubbles. In this view, bubbles produced at early stages should be discarded not to saturate the traps before reaching steady state, and the bubble flow should be redirected towards the traps upon pressure stabilization. Besides, the applied guiding method should not alter the pressure regime inside the chip. Therefore, pushing and pulling the liquids along with the use of the valves should be avoided.

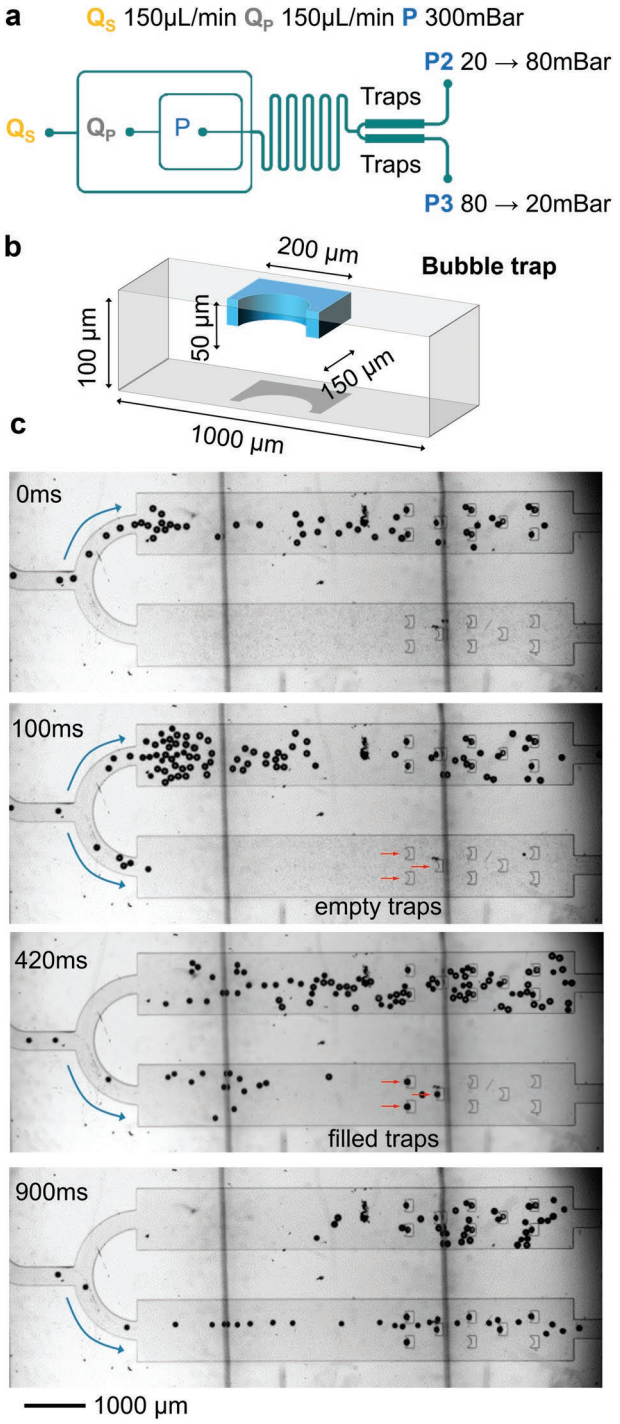

Figure 2. Direction and trapping of particle-stabilized bubbles by backpressure inversion. a) Microfluidic chip and experimental conditions. b) Design of bubble trap. c) High-speed microscopy images of flow alternation (blue arrows) and bubble trapping (red arrows). Outer phase (Qs) DMSO, middle phase (Qp): Pd@SiO_2-F17 (5 wt% in 1-octanol), temperature 80 °C.

The proposed solution here is to use backpressure to navigate the flow in one of the chip's outputs (**Figure 2**a). The microfluidic chip possesses two identical observation chambers including arrays of bubble traps (Figure 2b) and inspired by the earlier work of Di Carlo et al.[11] The chip has low hydrodynamic resistance and limited clogging owing to the big gap size while being able to trap a broad variety of bubble sizes. A first flow is directed towards the output with lower counterpressure (P2, for instance). After reaching steady state, the backpressures P2 and P3 are inversed, and the bubble flow is redirected towards the bottom chamber. The empty traps are then filled with monodisperse bubbles (Figure 2c). In an ideal situation, due to the identical geometry of both outputs, no pressure change should occur in the flow-focusing geometry upon backpressure inversion. Nonetheless, in reality, the output tubes are not identically filled with bubbles, resulting in a slightly different hydrodynamic resistance. At low ΔP between the liquid and gas, this results in slightly different bubble sizes before and after flow alteration (Figure 2c). This effect is not present if higher gas pressure is used (Figure S11, Supporting Information). However, due to the high stability of particle-stabilized bubbles, it is not trivial to clean the bubble traps once they are filled ("Old bubble" in Figure S11, Supporting Information).

In addition to the ΔP, control of the bubble size in the microfluidic chip after stopping the flow is also challenging. While monodisperse bubbles are produced underflow, relaxation of the system after interrupting the liquid flow and setting the gas pressure to zero results in polydisperse bubbles that fill preferentially the trap zones with lower back pressure (Figure S12, Supporting Information). At the same time, the trap zones with higher backpressure experience backflow, bringing some bubbles from the output tubes. Despite these shortcomings, we succeeded in keeping monodisperse bubbles in the traps for a vast majority of experiments, allowing further implementation of catalytic tests in individual bubbles as described in the following section. Better results may be achieved using a program-controlled variation of liquid flow rates and gas pressures assuring zero flow in the trap zone of interest upon stop flow.

2.4. Monitoring of Catalytic Events

With the microfluidic traps in hand, we monitored catalytic events on individual bubbles stabilized by surface-active catalytic particles using the aerobic oxidation of 2',7'-dichlorodihydrofluorescein (H_2DCF) into highly fluorescent 2',7'-dichlorofluorescein (DCF) as model reaction (**Figure 3** and Figure S13a, Supporting Information). Commercially available 2',7'-dichlorodihydro fluorescein diacetate (H_2DCF-DA) is commonly used in biology to measure the oxidative stress in living cells, where it is first deesterified by esterase enzyme.[12] The use of NaOH aqueous solution for the same purpose was also reported.[13] Due to the low solubility of inorganic bases in DMSO, we chose potassium tert-butoxide (*t*-BuOK) instead. Base addition results in the apparition of a characteristic band centered at 330 nm in the UV–vis spectra that confirms H_2DCF formation (Figure S13b, Supporting Information). The band intensity increases with the base concentration, especially in the range of 1–5 mM. Cleavage of the ester bond appears to be extremely fast as no band evolution is observed at longer reaction times (Figure S13c, Supporting Information). A weak band appears at 530 nm which can be attributed to the oxidized product (DCF).

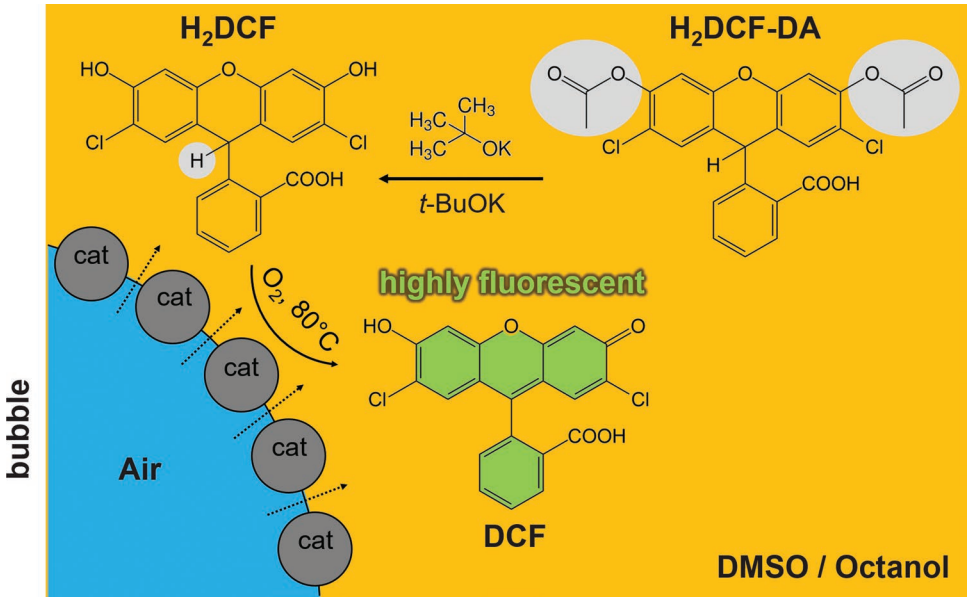

Figure 3. Scheme of the catalytic test: two-step formation of 2',7'-dichlorofluorescein (DCF); deesterification of 2',7'-dichlorodihydrofluorescein diacetate (H_2DCF-DA) promoted by *t*-BuOK occurs in the bulk solvent, followed by catalytic oxidation of the intermediate product on the surface of a bubble armored with surface-active catalytic particles.

In the next step, the same chip design as in Figure 2a was used to study the catalytic reaction over a trapped air bubble. In the first set of the experiments, 1 mM H_2DCF-DA and 10 mM *t*-BuOK in DMSO ("bad" solvent) were used as external phase, while the particles were dispersed in 1-octanol ("good" solvent) as the middle phase. Dye oxidation occurs in all experiments regardless of the particle concentration (range 1–5 wt.%) (Figure S14, Supporting Information). A fluorescent signal appears mainly at the G–L–S interface with only slight increase in the background level. Interestingly, oxidation occurs predominantly on larger bubbles (resulting from the coalescence of primary bubbles), while no fluorescence is observed on smaller monodisperse and more stable bubbles at the timescale used (Figure S14b, Supporting Information). These observations are consistent with a previous work, where highly stable foams revealed lesser catalytic activity compared to foams with intermediate stability due to restricted gas diffusion within the particle layer at the G–L interface.[2] At 1 wt% particle concentration, we observe leaching of the fluorescent product from the bubbles (Figure S15, Supporting Information). This effect is less visible at 2 wt% and completely vanishes at 4–5 wt% particle concentration. These results suggest that even at low interfacial surface coverage by particles, the mass transfer can be significantly affected by the particle layer. Also, fast formation of the fluorescent product is observed in the thin film on the glass surface, where a loose particle layer can allow faster gas diffusion.

Analysis of the mean fluorescence intensity across the observation chamber highlights several phenomena. All experiments exhibit an induction period up to ≈40 s with a slow increase in fluorescence intensity, followed by a period of much faster growth (Figure S14a, Supporting Information). Neat deceleration is apparent for experiments with 2 and 3 wt% particle concentrations after 90 s. It can also be noticed that fluorescence in the bulk liquid increases between the experiments suggesting oxidation of H_2DCF in the feeding syringe. To avoid this phenomenon and allow proper comparison between the experiments, deesterification was conducted directly in the microfluidic chip. To this aim, in a second set of experiments, the base (10 mM *t*-BuOK) was added to the middle phase containing catalytic particles, while the external phase contained H_2DCF-DA alone (**Figure 4**). As expected, no variation of fluorescence in the bulk is observed for all experiments. Oxidation on the bubble is similar to that discussed above, that is, the reaction occurs preferentially on larger polydisperse bubbles, whereas smaller monodisperse bubbles (marked with red arrows) exhibit no reactivity (Figure 4a,b). The initiation period is followed by a fast fluorescence intensity growth and deceleration (Figure 4c). The fluorescence of the liquid bulk remains constant suggesting no photooxidation. The highest reaction rates are observed on clusters of catalytic particles (red spots in Figure 4, bottom right).

To explain the difference in catalytic performance between primary monodisperse bubbles and their larger coalesced counterparts, it is useful to visualize the particle layer structure of both objects. This can be done using non-catalytic fluorescent SiO_2-C18-RhB particles in the same solvent system (**Figure 5**). It can be seen that the particle layer in smaller monodisperse bubbles is extremely dense and thick. This thick layer is expected to block gas diffusion and to render very stable bubbles inactive. On the contrary, in the case of coalesced bubbles, the particle shell is incomplete, allowing gas and liquid diffusion while providing some catalytic centers for the reaction to occur. These observations are consistent with the data obtained for the bulk system.[2]

3. Conclusion

In summary, we developed microfluidic traps to produce and store particle-stabilized bubbles in organic solvents at elevated

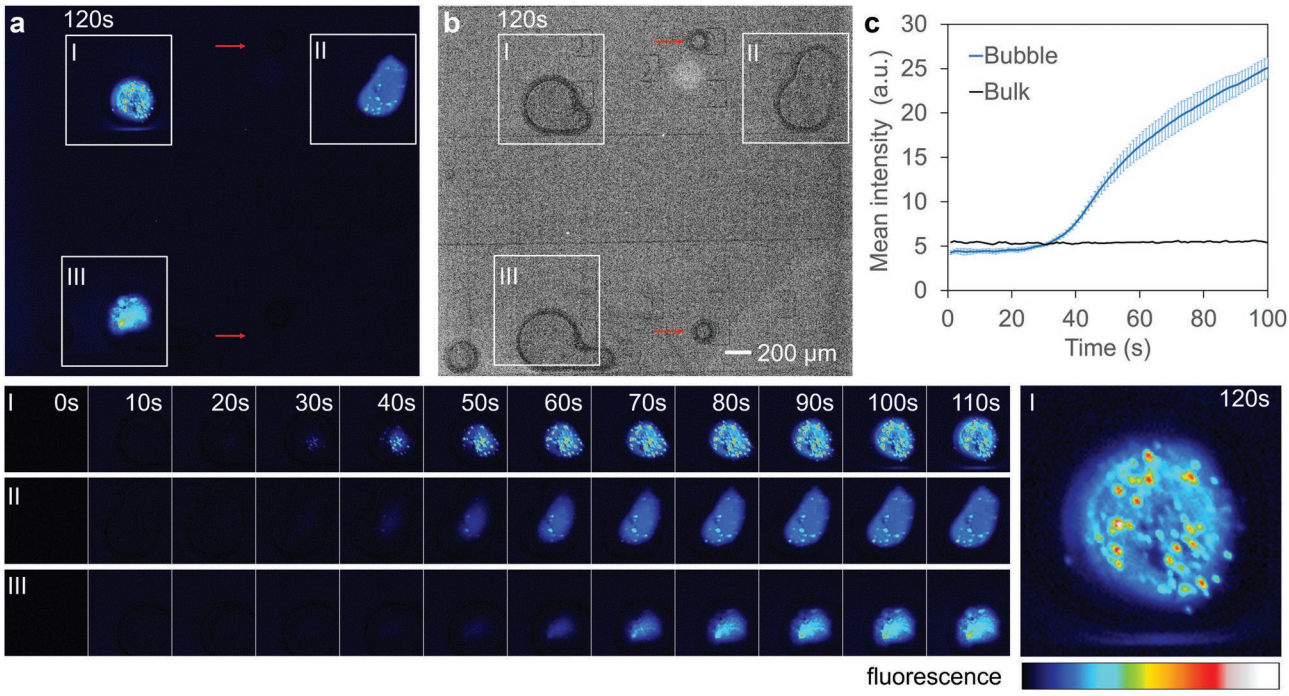

Figure 4. Catalysis on a particle-stabilized bubble. a) Fluorescence images of the microfluidic chip after 2 min. I–III) Time-lapse of corresponding chip regions. b) Same as (a) but in the grayscale representation and with busted image brightness to show all bubbles present in the chip. Stable monodisperse bubbles indicated with arrows produce no fluorescent signal. c) Plots of mean fluorescence intensity across bubbles and in the bulk as a function of time. Curves of mean fluorescence intensity for different bubbles are time-shifted matching the fluorescence apparition time. Outer phase (Qs = 150 µL min^{-1}): H_2DCF-DA (1 mM in DMSO), middle phase (Qp = 150 µL min^{-1}): Pd@SiO_2-F17 (4 wt% in 1-octanol with 10 mM *t*-BuOK), air pressure P = 400 mbar, temperature 80 °C.

temperatures, and study catalytic events. The solvent composition was used to adjust in situ the particle wettability. This allowed combining the colloidal stability of the particles with their surface activity. Backpressure inversion was efficient to direct the bubble flow without impacting the bubble size. Bubble generation in the colloidal dispersion and subsequent injection of co-solvent showed better results than when two phases were inversed. Bubble trapping was achieved with traps of simple design. Stop flow, however, remains a challenge as residual pressure in the system leads to polydisperse bubbles which can access the trapping zone. We then used fluorescent probe 2',7'-dichlorodihydrofluorescein diacetate to monitor catalytic events in the organic phase after deesterification with a organic base. Only large bubbles loosely covered by catalytic particles showed reactivity while monodisperse armored bubbles remained inert.

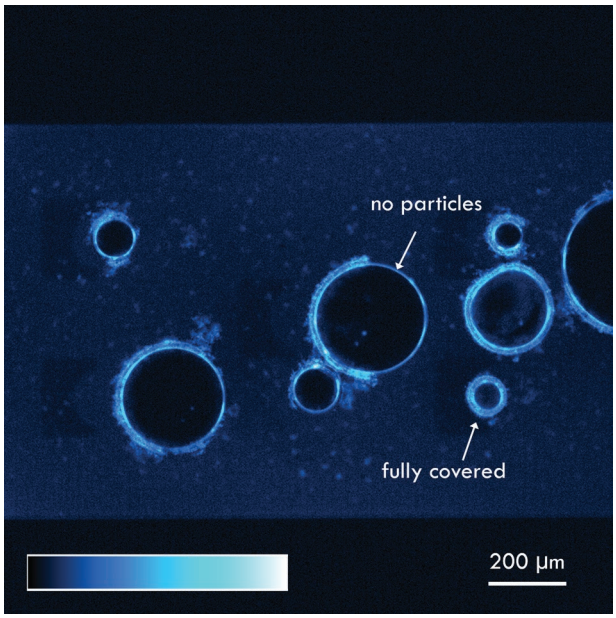

Figure 5. Fluorescent image of air bubbles in Octanol/DMSO (1:1) stabilized by fluorescent (rhodamine B) non-catalytic SiO_2-C18-RhB silica particles.

The traps developed in this study may be applied to a variety of heterogeneous reactive systems. Fluorescence can allow reaction mapping and, contrary to IR or Raman spectroscopy, does not require special materials for chip manufacture. Microfluidics allows systematic production and manipulation of monodisperse bubbles which can be used to acquire statistical data on the system reactivity and evaluate the impact of bubble size, packing, and particle coverage of the gas-liquid interface. Moreover, using tracers and temperature-sensitive probes, local heat and mass transfer phenomena can be studied in parallel.

4. Experimental Section

Materials: Tetraethyl orthosilicate (TEOS, 98%), 1H,1H,2H,2H-perfluorodecyltriethoxysilane (PFDTES, 97%), n-octadecyltriethoxysilane

(ODTES, 98%), (3-mercaptopropyl)triethoxysilane (MPTES, > 80%), (3-aminopropyl)triethoxysilane (APTES, 99%), ammonium hydroxide solution (28%–30%), anhydrous ethanol (99.9%), palladium(II) acetate (98%), potassium borohydride (KBH_4, 98%) and rhodamine B isothiocyanate (mixed isomers), all supplied by Sigma-Aldrich, were used for the synthesis of catalytic silica particles. Dimethylpolysiloxane (PDMS, Sylgard 184), hexamethyldisilazane (HMDS, > 99%), (poly(ethylene glycol) methyl ether acrylate (PEGMEA, > 99.5%), all purchased at Sigma-Aldrich, was used for preparing the microfluidic chips. Dimethyl sulfoxide (DMSO, 99.9%), 1-octanol (99%), and 2',7'-dichlorodihydrofluorescein diacetate (H_2DCF-DA, ≥ 97%), also procured from Sigma-Aldrich, were used for preparing the bubbles and conducting the catalytic tests. All the chemicals were used as received without further purification.

Characterization Methods: The bulk metal composition of the catalysts was analyzed by inductively coupled plasma on an Activa (Horiba Jobin-Yvon) optical emission spectrometer. Before analysis, the dried ground sample (≈10 mg) was dissolved in 1.5 mL of concentrated aqua regia and 250 µL of a 48% hydrofluoric acid (HF) solution. The solution was heated at 493 K and sonicated for 30 min. After digestion, a solution containing a mixture of the complexing and buffering agents (UNS-1 solution, Inorganic Ventures) was used to deactivate excess HF by increasing the pH to 7.5–8.0 and maintaining the solubility of the sample by complexation. The solutions were kept under mild stirring and the volume was adjusted to 50 mL using ultrapure water before analysis.

The thermal profiles were measured on a TGA/DSC 3+. The catalysts (≈10 mg in a 100 µL alumina crucible with an alumina lid) were treated from 25 to 600 °C with a heating rate of 10 °C min^{-1} under an airflow of 30 mL (STP) min^{-1}.

The Fourier-transform infrared (FTIR) spectra of particles dispersed in KBr (4 mg of catalyst in 100 mg of KBr) were measured from 500–4000 cm^{-1} in a PerkinElmer One FTIR instrument with 4 cm^{-1} resolution. For each spectrum, 30 scans were measured.

The morphology of the silica particles and Pd nanoparticles, as well as the particle size distributions, was measured by HR-TEM on a TEM Talos F200S G2 (200 kV) microscope equipped with an S-FEG (Field Electron Gun). The images were analyzed by ImageJ software. At least 200 particles were counted for the statistic chart. In the analyses, we assumed that the particles are spherical in shape

The solid-state ^{19}F, ^{13}C, and ^{29}Si NMR MAS spectra were recorded on a Bruker AVANCE III 600 WB spectrometer operating at 600 MHz resonance frequency equipped with a 4 mm standard probe spinning at 25 kHz. The chemical shifts were referenced to $CFCl_3$ and adamantane ($\delta CH_2 = 38.5$ ppm).

X-ray photoelectron spectroscopy (XPS) was performed on a Thermo Scientific K-Alpha+ XPS instrument equipped using a micro-focused monochromatic Al Kα X-ray source (1486.6 eV).

Synthesis of Fluorinated Silica Particles: Fluorinated organosilica particles were synthesized by the Stöber method using 1H,1H,2H,2H-perfluorodecyltriethoxysilane (PFDTES), (3-mercaptopropyl) triethoxysilane (MPTES) and tetraethylorthosilicate (TEOS) precursors, with MPTES/PFDTES and TEOS/PFDTES molar ratios of 1:1 and 16:1, respectively. The samples were loaded with Pd nanoparticles by wet impregnation using an ethanol solution of $Pd(OAc)_2$. The final Pd-loaded particles were denoted as Pd@SiO_2-F17.

In a typical experiment, 2 mL of TEOS, 5.6 mL of deionized water, and 3.2 mL of ammonia were dissolved in 40 mL of ethanol at 40 °C for 5 min. Then, 0.135 mL of MPTES and 0.25 mL of PFDTES were added to the solution. The reaction proceeded at 40 °C for 30 min, and the mixture was subsequently centrifuged to collect the modified particles, which were washed with ethanol three times. The collected solid was dried at 80 °C for 10 h.

For Pd loading, 300 mg of silica nanoparticles were added to 20 mL of ethanol containing 20 mg of $Pd(OAc)_2$. The dispersion was stirred mildly at room temperature for 2 h. Then, the particles were isolated by centrifugation and were reduced with 20 mg KBH_4 dissolved in 20 mL of ethanol. After mild stirring for 3 h at room temperature, the solid was isolated by centrifugation, washed four times with ethanol, and dried at 80 °C for 10 h.

SiO_2-C18-RhB was synthesized by a similar method: 2 mg rhodamine B isothiocyanate and 20 µL APTES are pre-prepared by stirring in 5 ml ethanol solution for one night. 2 mL of TEOS, 5.6 mL of deionized water and 3.2 mL of ammonia were dissolved in 40 mL of ethanol at 40 °C for 5 min. Then, the pre-prepared 5 mL ethanol solution and 1.8 mL of ODTES were added to the solution. The reaction proceeded at 40 °C for 3 h, and the mixture was subsequently centrifuged to collect the modified particles, which were washed with ethanol three times. The collected solid was dried at 80 °C for 10 h.

Properties of Fluorinated Silica Particles: The fluorinated particles were first inspected by HRTEM (Figure S1, Supporting Information). The particles consisted of a silica core and a fluorinated shell. The mean particle size was about ≈300 nm (Figure S2a, Supporting Information). Palladium nanoparticles, with a mean size of 5.2 nm, were well dispersed on the particles (Figure S2b, Supporting Information). Palladium loading was 1.78 wt% as determined by ICP-OES.

TG analysis of the particles before and after Pd impregnation showed a small weight loss until 150 °C (about 5%), which was attributed to water desorption (Figure S3, Supporting Information). The parent fluorinated silica particles exhibited a sharp weight loss in the range of 400–500 °C, which became broader (from 220 to 430 °C) after Pd impregnation. The weight loss after Pd loading was 23%, while the weight loss/F ratio (determined by TGA and ICP-EOS respectively) was 1.53 matching the expected ratio in PFDTES (1.6).

The surface composition of the particles was analyzed by FTIR spectroscopy (Figure S4, Supporting Information). Typical bands of silica appear at 1100 and 800 cm^{-1} that were assigned to asymmetric stretching and bending vibrations of Si–O–Si bonds, respectively.[14] Two additional bands at 3650 and 1610 cm^{-1} were indicative of symmetric stretching and bending vibrations of free Si–OH groups, respectively.[14] A broad band appeared in the range 3000–3500 cm^{-1} belonging to Si–OH groups interacting with adsorbed water, confirming the partial hydrophilic behavior of the particles. Characteristic bands ascribed to stretching modes of C-Si and C-F (CF_2/CF_3) bonds in the fluorocarbon chain appeared at 913, 1171, and 1237 cm^{-1}.[14] Additional bands at 710 and 670 cm^{-1} were attributed to symmetric stretching bands of CF_3 groups.[15] Bands ascribed to the carbon skeleton appeared at 1610 cm^{-1} due to asymmetric stretching modes of C–C groups, and at 2934 and 1462 cm^{-1} due to C–H stretching and bending vibrations.[15] No band corresponding to the stretching vibration of S–H groups (2560 cm^{-1}) wasobserved,[16] which could be explained by the low loading of mercaptopropyl groups on the particles.

XPS analysis showed characteristic Pd 3d core-level features (Figure S5, Supporting Information). The $3d_{5/2}$ and $3d_{3/2}$ spin-orbit bands after reduction could be deconvoluted into two bands centered at 335.1/337.3 eV (Pd 3d5/2) and 340.3/342.6 eV (Pd 3d3/2), respectively, which were indicative of Pd^0 and $Pd^{II}O$ species on the particles.[17] The C1s XPS core-level region showed bands in the range 286.5–293.5 eV that were consistent with the presence of CF_3, CF_2, and CF_2–CH_2 groups.[18] Additional bands in the range 283.0–286.5 eV were indicative of C–C and CH_2 bonds,[19] as well as bands at 293.7 and 296.5 eV, which were reminiscent of K^+ cations from KBH_4.

Fabrication of Microfluidic Traps: A two-level master form was prepared as following. First, a 3″ silicon wafer was heated at 150 °C for 1 h to remove adsorbed water. It was then silanized with hexamethyldisilazane (HMDS, Sigma-Aldrich) at 95 °C for 1 h. The first level of SU8 3050 (Microchem Inc.) was spin coated (APT GmbH SPIN150) to the height of 50 µm. After a pre-baking step (95 °C for 15 min), SU8 was subjected to UV light for a period of 8 s through a film mask (Cad/Art Services, Inc) with the requisite design. This was followed by a post-baking step (95 °C for 5 min). The same procedure was repeated for the second layer. Development was done in PEGMEA (Poly(ethylene glycol) methyl ether acrylate for 5 min using an ultrasonic bath (Ultrasonic Cleaner, 45 kHz, VWR).

Microfluidic chips were produced by heat curing (65 °C for 2 hours) PDMS and curing agent mixture (10:1) on the master form. Cured PDMS was peeled and cut into individual chips. Fluidic access holes

were punched at respective inlets and outlets using a 1 mm biopsy puncher (Kai Industries). Finally, the PDMS chips were bonded onto a glass coverslip using an air plasma treatment (Plasma Cleaner, Diener electronic GmbH & Co. KG) at 500–600 mbar for 1 min.

Experimental Set-Up: A homemade heating stage was fabricated by gluing transparent heating film (MINCO, 7 cm length, 3 cm width) to the glass slide (76 × 51 mm). A CT325 temperature controller (MINCO) equipped with a thermocouple was used to set and maintain the required temperature. The device was calibrated with an external thermocouple inserted in the PDMS chip.

The flow rate of the liquid phases was controlled with a NEMESYS syringe pump (CETONI GmbH) equipped with gas-tight glass syringes (VWR). The air pressure was controlled with a 1 bar MFCS™ EZ pressure controller (FLUIGENT SA).

High-speed acquisition of the microfluidic device was done using an Olympus IX73 inverted microscope equipped with a Miro Lab 310 high-speed camera. For fluorescence imaging, the chip was illuminated with an X-Cite-120Q lamp (Excelitas Technologies®).

Supporting Information

Supporting Information is available from the Wiley Online Library or from the author.

Acknowledgements

This study was funded by the ERC grant Michelangelo (contract number #771586).

Conflict of Interest

The authors declare no conflict of interest.

Data Availability Statement

The data that support the findings of this study are openly available in HAL at https://hal.archives-ouvertes.fr, reference number 0.

Keywords

catalysis, fluorescence, microfluidics, organic solvents, pickering foam

Received: April 5, 2022
Revised: June 7, 2022
Published online:

[1] a) K.-D. Henkel, in *Ullmann's Encyclopedia of Industrial Chemistry*, (Eds: W. Gerhartz, B. Elvers), Wiley-VCH Verlag GmbH & Co. KGaA, Weinheim, Germany **2000**; b) Y. T. Shah, *Gas-Liquid-Solid Reactor Design*, McGraw-Hill, New York **1979**; c) P. Trambouze, J. P. Euzen, *Chemical Reactors – from Design to Operation*, Technip Editions, Paris **2004**; d) M. P. Dudukovic, Ž. V. Kuzeljevic, D. P. Combest, in *Ullmann's Encyclopedia of Industrial Chemistry*, (Eds: W. Gerhartz, B. Elvers), Wiley-VCH Verlag GmbH & Co. KGaA, Weinheim, Germany **2013**, p. 1.
[2] S. Zhang, D. Dedovets, A. Feng, M. Pera-Titus, *J. Am. Chem. Soc.* **2022**, *144*, 1729.
[3] D. Dedovets, Q. Li, L. Leclercq, V. Nardello-Rataj, J. Leng, S. Zhao, M. Pera-Titus, *Angew. Chem., Int. Ed.* **2021**, *61*, 202107537.
[4] A. L. Fameau, A. Saint-Jalmes, *Adv. Colloid Interface Sci.* **2017**, *247*, 454.
[5] a) M. H. Lee, V. Prasad, D. Lee, *Langmuir* **2010**, *26*, 2227; b) H. Chen, J. Li, J. Wan, D. A. Weitz, H. A. Stone, *Soft Matter* **2013**, *9*, 38.
[6] S. E. Friberg, *Curr. Opin. Colloid Interface Sci.* **2010**, *15*, 359.
[7] J. Il Park, Z. Nie, A. Kumachev, A. I. Abdelrahman, B. P. Binks, H. A. Stone, E. Kumacheva, *Angew. Chem., Int. Ed.* **2009**, *48*, 5300.
[8] J. C. Baret, L. A. Chacon, *ChemSystemsChem* **2019**, *1*, 16.
[9] A. P. Kotula, S. L. Anna, *Soft Matter* **2012**, *8*, 10759.
[10] J. Nilsson, M. Evander, B. Hammarström, T. Laurell, *Anal. Chim. Acta* **2009**, *649*, 141.
[11] a) D. Di Carlo, N. Aghdam, L. P. Lee, *Anal. Chem.* **2006**, *78*, 4925; b) J. Nilsson, M. Evander, B. Hammarström, T. Laurell, *Anal. Chim. Acta* **2009**, *649*, 141.
[12] A. Gomes, E. Fernandes, J. L. F. C. Lima, *J. Biochem. Biophys. Methods* **2005**, *65*, 45.
[13] a) M. J. Reiniers, R. F. Van Golen, S. Bonnet, M. Broekgaarden, T. M. Van Gulik, M. R. Egmond, M. Heger, *Anal. Chem.* **2017**, *89*, 3853; b) R. Bresolí-Obach, L. Busto-Moner, C. Muller, M. Reina, S. Nonell, *Photochem. Photobiol.* **2018**, *94*, 1143.
[14] V. I. Chukin, G. D. Malevich, *J. Appl. Spectrosc.* **1977**, *26*, 223.
[15] A. Shahabadi, S. M. S. Rabiee, H. Seyed, S. M. Mokhtare, A. Brant, *J. Membr. Sci.* **2017**, *537*, 140.
[16] J. J. Senkevich, C. J. Mitchell, G.-R. Yang, T.-M. Lu, *Langmuir* **2002**, *18*, 1587.
[17] a) K. Engler, B. H. Lindner, D. Lox, E. S. Schafer-Sindlinger, A. Ostgathe, *Stud. Surf. Sci. Catal.* **1995**, *96*, 441; b) K. Otto, L. P. Haack, J. E. DeVries, *Appl. Catal., B* **1992**, *1*, 1; c) P. A. Deshpande, M. S. Hegde, G. Madras, *Appl. Catal., B* **2010**, *96*, 83.
[18] X. L. Zhu, S. B. Liu, B. Y. Man, C. Q. Xie, D. P. Chen, D. Q. Wang, T. C. Ye, M. Liu, *Appl. Surf. Sci.* **2007**, *253*, 3122.
[19] L. S. Kibis, A. I. Titkov, A. I. Stadnichenko, S. V. Koscheev, A. I. Boronin, *Appl. Surf. Sci.* **2009**, *255*, 9248.